C h a p t e r 4

Enhanced Ammonia Oxidation Catalysis by a Low-Spin Iron Complex Featuring *Cis* Coordination Sites

Adapted from:
Zott, M. D.; Peters, J. C.
J. Am. Chem. Soc. **2021**, *143*, 7612–7616.
DOI: 10.1021/jacs.1c02232
.

4.1 Introduction

Ammonia is produced at industrial scale for use in fertilizer and chemical synthesis,[1,2] but could become a promising carbon-free fuel if its selective and efficient catalytic oxidation to nitrogen can be achieved. Catalysts sufficiently active and stable for fuel cell applications are still needed.[2,3,4] Platinum-based materials, perhaps the current best current candidates,[5,6,7] suffer from low current densities due to side reactions that can result at moderate applied bias.

Molecular systems offer several advantages with respect to fundamental studies that address both activity and selectivity in AO.[8] The first molecular AO catalysts were reported in 2019.[9,10,11,12,13] Thus far, ruthenium catalysts have shown the highest turnover number[14] (TON; ~120 for $[(TMP)Ru(NH_3)_2]^{2+}$ using phenoxyl HAA reagents),[13] and the lowest demonstrated onset potential for electrocatalysis (E_{onset} = 0.04 V vs Fc/Fc^+ for $[(bpydma)(tpy)Ru(NH_3)]^{2+}$; TON = 2).[9] We reported a distinct example of a first-row metal electrocatalyst, $[(TPA)Fe(NH_3)_2]OTf_2$, with a TON of 16 and a comparatively very fast rate (10^7 $M^{-1}\cdot s^{-1}$), but requiring a substantial E_{onset} bias of 0.7 V (all potentials are reported vs Fc/Fc^+).[12]

To improve on the AO activity of $[(TPA)Fe(NH_3)_2]OTf_2$, we targeted an iron system that would display enhanced catalyst stability while showing higher activity at a lower applied bias. Catalyst degradation with $[(TPA)Fe(NH_3)_2]OTf_2$ appears to initiate from substitution of the TPA ligand, an equilibrium process under the catalytic conditions that is likely favored by the presence of a large excess of NH_3. The extent of TPA displacement

from [(TPA)Fe(NH_3)$_2$]OTf_2 is likely increased by the complex's dominant high-spin population (S = 2) at RT, which results in more labile M–L bonds.

For the present system, given that the initial iron species in bulk solution during catalysis is [(TPA)Fe(NH_3)$_2$]OTf_2, we explored whether modifying the auxiliary ligand (L_{aux}) in such a fashion so as to support a low-spin (L_{aux})Fe(II)–NH_3 adduct might limit substitution by NH_3 and hence enhance overall stability, while maintaining high catalyst activity. We decided to replace the weak-field tertiary amine donor of TPA, along with one of its pyridyl arms, with a bipyridine ligand (Scheme 4.1); bipyridine has similar σ-donating properties to pyridine but enhanced π-accepting properties.[15,16,17] We also sought to maintain the *cis*-labile sites present in [(TPA)Fe(NH_3)$_2$]OTf_2,[18,19,20,21] which may facilitate intramolecular N–N bond formation. A rigid ligand containing each of these characteristics, bpyPy$_2$Me (Scheme 4.1), has been reported,[22] as has its iron(II) complex, [(bpyPy$_2$Me)Fe(MeCN)$_2$]OTf_2. The latter has been studied in the context of alkane oxidation.[21]

Scheme 4.1. Targeting enhanced Fe-mediated AO via an alternative auxiliary ligand strategy.

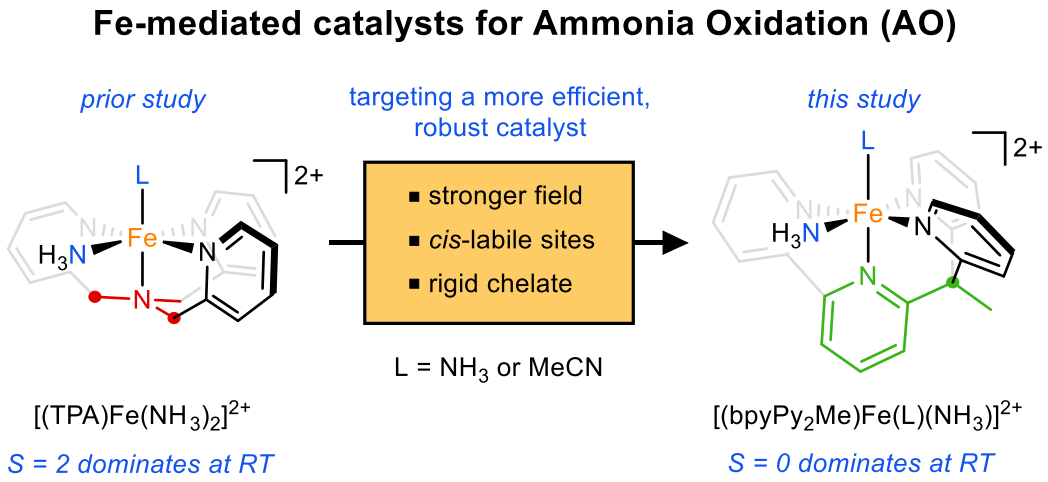

4.2 Results and Discussion

We first compared the electronic structure of both [(TPA)Fe(MeCN)$_2$]OTf$_2$ and [(bpyPy$_2$Me)Fe(MeCN)$_2$]OTf$_2$ in the presence of NH_3 in solution by the Evans method, using trimethoxybenzene as an inert reference signal. At room temperature in the absence of NH_3, both systems display NMR spectra with resonances in the typical diamagnetic window, and bulk magnetic moments of 0.7–0.8μ_B (see SI), indicating a dominant low-spin population. In the presence of 75 equivalents NH_3 (~0.8 M at NMR concentrations), however, the solution prepared with [(TPA)Fe(MeCN)$_2$]OTf$_2$ gives rise to a spin-only magnetic moment of 5.2μ_B, indicative of a fully populated S = 2 state. By contrast, under identical conditions, a solution prepared with [(bpyPy$_2$Me)Fe(MeCN)$_2$]OTf$_2$ produces a bulk magnetic moment of 1.2μ_B. Assuming a mixture of S = 0 and S = 2 species at spin-only values, this moment corresponds to a 94:6 mixture in favor of the low-spin derivative in the presence of NH_3.

To assess the stability of [(bpyPy$_2$Me)Fe(MeCN)$_2$]OTf$_2$ to substitution by NH_3 in MeCN, we monitored its speciation by UV-vis spectroscopy while titrating in NH_3. A monotonic decrease in the absorbance for [(bpyPy$_2$Me)Fe(L)$_2$]OTf$_2$ (L = MeCN, NH_3), as well as a loss of isosbestic behavior, becomes discernable in the presence of > 600 equivalents NH_3 (see SI). By contrast, [(TPA)Fe(MeCN)$_2$]OTf$_2$ begins showing demetallation with > 200 equivalents NH_3.[12]

We next assessed catalytic AO by [(bpyPy$_2$Me)Fe(MeCN)$_2$]OTf$_2$ via cyclic voltammetry (CV) and controlled potential coulometry (CPC) using boron-doped diamond (BDD) working electrodes. CV of [(bpyPy$_2$Me)Fe(MeCN)$_2$]OTf$_2$ with added NH_3 as

substrate shows a precatalytic one-electron feature E_1 at 0.24 V and an irreversible multi-electron E_2 wave at 0.79 V (Figure 4.1; see SI for DPV data), which replace the reversible one-electron wave observed in the absence of NH_3 ($E_{1/2}$ = 0.82 V); this behavior mirrors that of $[(TPA)Fe(NH_3)_2]OTf_2$.[12] The catalytic onset potential of 0.45 V for $[(bpyPy_2Me)Fe(MeCN)_2]OTf_2$ is ~250 mV cathodic of that for $[(TPA)Fe(MeCN)_2]OTf_2$, and the catalytic current is ~fourfold higher. By contrast, applying less potential bias most typically results in a concomitant decrease in catalytic current.[23,24]

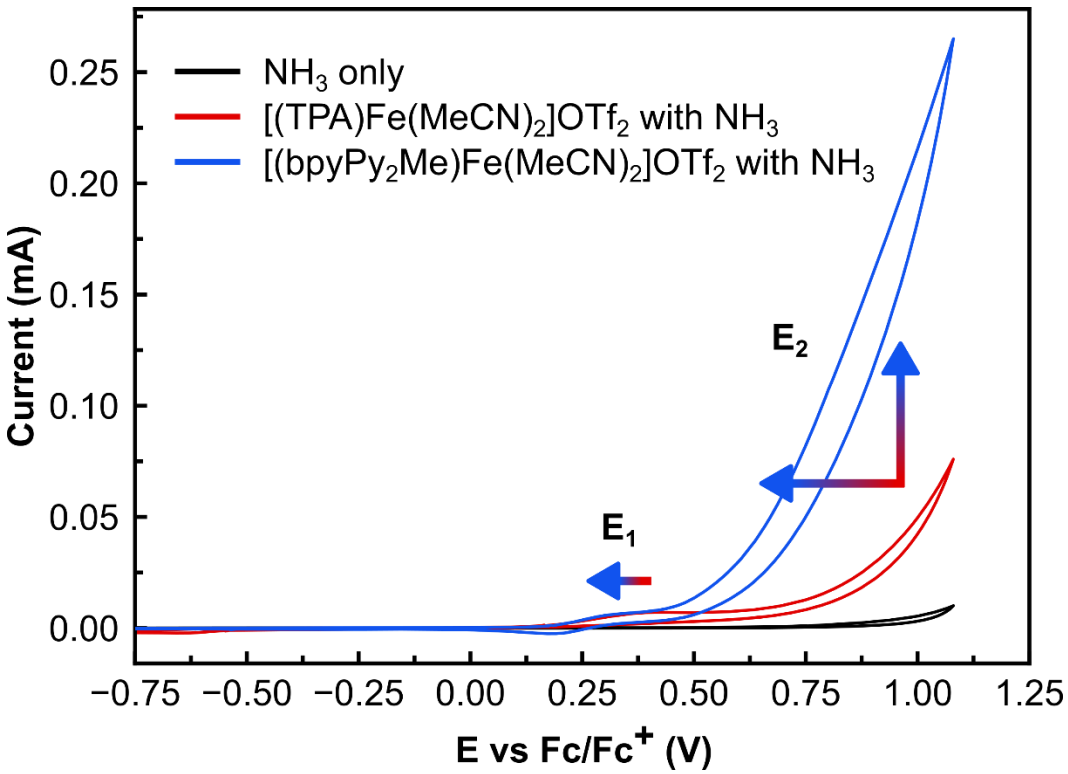

Figure 4.1. CV of MeCN solutions containing 0.2 M NH_3 (400 equivalents), 0.05 M NH_4OTf, and 0.5 mM $[(TPA)Fe(MeCN)_2]OTf_2$ or $[(bpyPy_2Me)Fe(MeCN)_2]OTf_2$ with BDD working, Pt counter, and 5 mM Ag/AgOTf reference electrodes.

CPC confirms that $[(bpyPy_2Me)Fe(MeCN)_2]OTf_2$ is a highly active AO catalyst. With a 0.05 mM $[(bpyPy_2Me)Fe(MeCN)_2]OTf_2$ solution containing 400 equivalents NH_3 in MeCN with NH_4OTf supporting electrolyte (0.05 M), holding the bias at 0.85 V produces

N_2 with a high faradaic efficiency (FE) of 87%. After 24 h, a TON of 93 (average of 4 runs; STD = 8) was measured. Furthermore, active catalyst remains after 24 h; a reload experiment was performed in which the BDD electrode was cleaned and the NH_3 concentration was reset to its original value; after an additional 24 h, another 56 equivalents N_2 were detected (average of 2 runs), resulting in a net TON of 149. With respect to TON, this value is a marked improvement on both the previously reported Ru AO electrocatalyst (TON of 2) and $[(TPA)Fe(MeCN)_2]OTf_2$ (TON of 16).[9,12] CPC with $^{15}NH_3$ (^{15}N = 99%) produces >90% $^{30}N_2$ by GC-MS, indicating NH_3 as the source of nitrogen in the liberated N_2. Post-catalysis, a thoroughly rinsed electrode showed no catalytic activity, under the same conditions but without added $[(bpyPy_2Me)Fe(MeCN)_2]OTf_2$.[25]

To probe mechanistic issues for the $[(bpyPy_2Me)Fe(MeCN)_2]OTf_2$ system, we further investigated the E_1 process. By CV, as the concentration of NH_3 is increased, the E_1 potential shifts cathodically. This is characteristic of an EC mechanism (single electron transfer followed by a chemical step).[26,27] For an EC mechanism in the observed kinetic regime (KE), the peak potential of such a process obeys Eq. 1 (Scheme 4.2). Two plausible stoichiometries are provided, involving either one or two molecules of NH_3 in the forward reaction (Scheme 4.2a and 4.2b, respectively). Plotting E_1 versus either $[NH_3]$ or $[NH_4^+]$ (Scheme 4.2c and 4.2d, respectively), the respective slopes support stoichiometries of two NH_3 in the forward reaction and one NH_4^+ in the backward reaction, matching Scheme 4.2b. Taking the iron species to be $[(bpyPy_2Me)Fe(MeCN)(NH_3)]OTf_2$, we thus propose that the product of this EC reaction is $[(bpyPy_2Me)Fe(NH_2)(NH_3)]OTf_2$, formed via substitution and net hydrogen atom abstraction. This behavior parallels $[(TPA)Fe(NH_3)_2]OTf_2$, which follows Scheme 4.2a at a nearly identical potential.[12]

Scheme 4.2. Evidence supporting an EC mechanism at the E_1 potential. Possible stoichiometries of the E_1 potential are shown in (a) and (b). Plots of E_1 potential versus the natural logarithm of (c) NH_3 or (d) NH_4^+ concentration for $[(bpyPy_2Me)Fe(MeCN)_2]OTf_2$.

$$E_{ox} = E^\circ_{ox} - \frac{RT}{nF} \ln \frac{k_{1f}[NH_3]^m}{k_{1b}[NH_4^+]}$$

$$= E^\circ_{ox} - m \times 0.026 \ln(k_{1f}[NH_3]) + 0.026 \ln(k_{1b}[NH_4^+]) \quad \textbf{(1)}$$

$$Fe^{II}\text{–}NH_3 + NH_3 \underset{k_{1b}}{\overset{k_{1f}}{\rightleftharpoons}} Fe^{III}\text{–}NH_2 + NH_4^+ + e^- \quad \textbf{(a)}$$

$$\begin{matrix} MeCN \\ | \\ Fe^{II}\text{–}NH_3 \end{matrix} + 2\ NH_3 \underset{k_{1b}}{\overset{k_{1f}}{\rightleftharpoons}} \begin{matrix} NH_2 \\ | \\ Fe^{III}\text{–}NH_3 \end{matrix} + NH_4^+ + MeCN + e^- \quad \textbf{(b)}$$

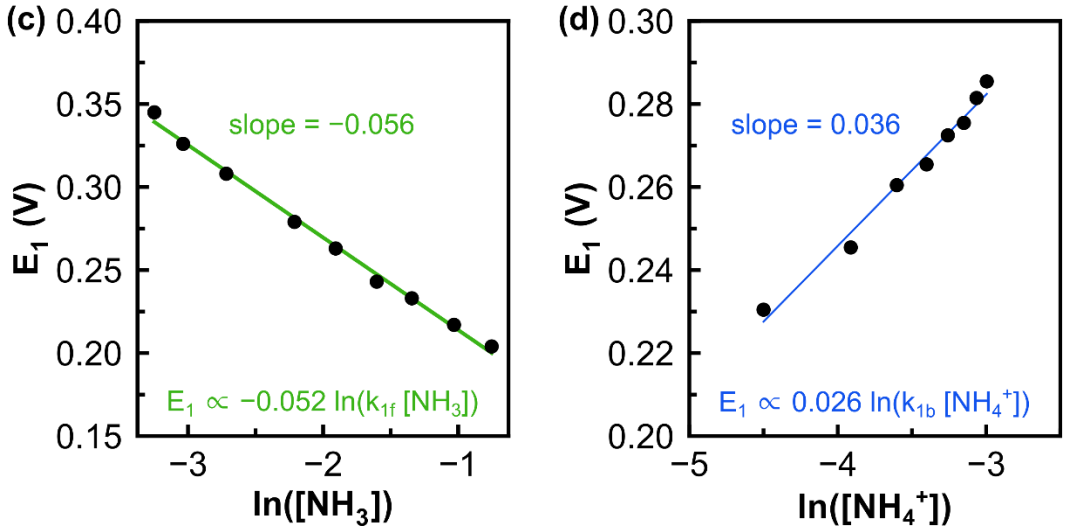

The iron speciation deduced from the above electrochemical data, favoring $[(bpyPy_2Me)Fe(MeCN)(NH_3)]OTf_2$ prior to E_1, is notionally consistent with a solid-state XRD study of a crystal grown from an ammoniacal MeCN solution (Figure 4.2). The short

Fe–N_{bpy} bond length *trans* to MeCN of 1.89 Å also underscores tight binding of the bpyPy_2Me ligand.

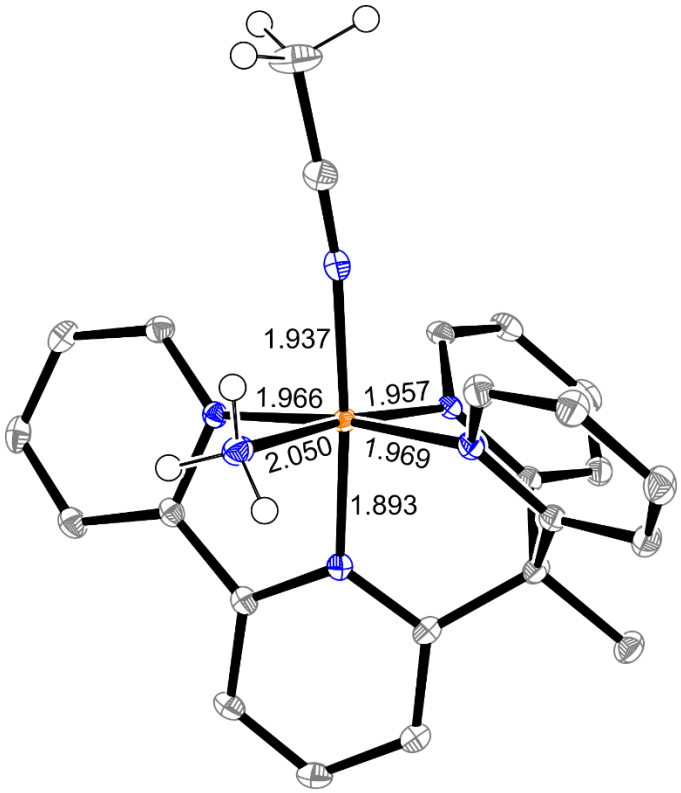

Figure 4.2. Solid-state crystal structure of [(bpyPy_2Me)Fe(MeCN)(NH_3)]OTf_2 at 100 K, with select bond lengths labeled in angstroms. Thermal ellipsoids are shown at 50% probability. Triflate counterions and L_{aux} hydrogen atoms are omitted for clarity.

To understand the character of the turnover-limiting E_2 step, we studied the rate dependence on [Fe] and [NH_3] concentrations. [(bpyPy_2Me)Fe(MeCN)(NH_3)]OTf_2 demonstrates first-order behavior for both [Fe] and [NH_3] (SI). The concentration ranges studied ([Fe] = 0.05–2 mM, [NH_3] = 0–0.5 M) span the conditions employed for both CV and CPC experiments. Using the foot-of-the-wave analysis with a standard EC_{cat} scheme to simplify the multi-electron, multi-proton wave, [28,29] the first-order dependence on iron was recapitulated; however, while a clear dependence on [NH_3] is evident from the FOWA,

ascertaining the quantitative dependence on [NH_3] is hindered by uncertainty in $E°_{cat}$ at high NH_3 concentrations. Still, we are able to compare the intrinsic AO reaction rates for $[(TPA)Fe(NH_3)_2]^{2+}$ and $[(bpyPy_2Me)Fe(MeCN)(NH_3)]^{2+}$. We previously reported a second-order rate constant (k'_{obs}) of $3.7 \times 10^7\ M^{-1} \cdot s^{-1}$ for $[(TPA)Fe(NH_3)_2]^{2+}$;[12] for the present catalyst $[(bpyPy_2Me)Fe(MeCN)(NH_3)]^{2+}$, the average k'_{obs} is $1.8 \times 10^9\ M^{-1} \cdot s^{-1}$. Thus, $[(bpyPy_2Me)Fe(MeCN)(NH_3)]^{2+}$ is ca. 1.5 orders of magnitude faster than $[(TPA)Fe(NH_3)_2]^{2+}$.

The aforementioned electrochemical data are limited in mechanistic utility with respect to the various steps that follow E_2, governing the pathway for N–N bond formation. Literature precedent for N–N formation in systems applied to AO, whether mono- or bimolecular in nature with respect to the metal complex, suggests two broad scenarios for consideration: (1) interaction of two nitrogen ligands (I2N), as via nitride,[8,11,30,31,32] imide, or amide[33,34] coupling, or (2) ammonia nucleophilic attack (ANA) on an electrophilic nitrido or imido ligand.[9,10] To begin to explore these issues for the present iron system, we have undertaken a theoretical study (Schemes 4.3, 4.4), using density functional theory due to the size of the present system, and the TPSS functional owing to its minimal bias for Fe^{2+} versus Fe^{3+} states.[35,36]

As an initial point of calibration, our chosen method reliably predicts the low-spin ground state of $[(bpyPy_2Me)Fe(MeCN)(NH_3)]^{2+}$ and also its E_1 potential (0.24 V calcd; see SI), which is analogous to that experimentally observed at 0.2 M NH_3. The latter result is encouraging as it involves both a change in oxidation state and a chemical step (to produce $[(bpyPy_2Me)Fe(NH_2)(NH_3)]^{2+}$, in accordance with our electrochemical data).

Scheme 4.3. Possible E_2 steps and calculated E (V) values. DFT-predicted ground spin-state values are shown.

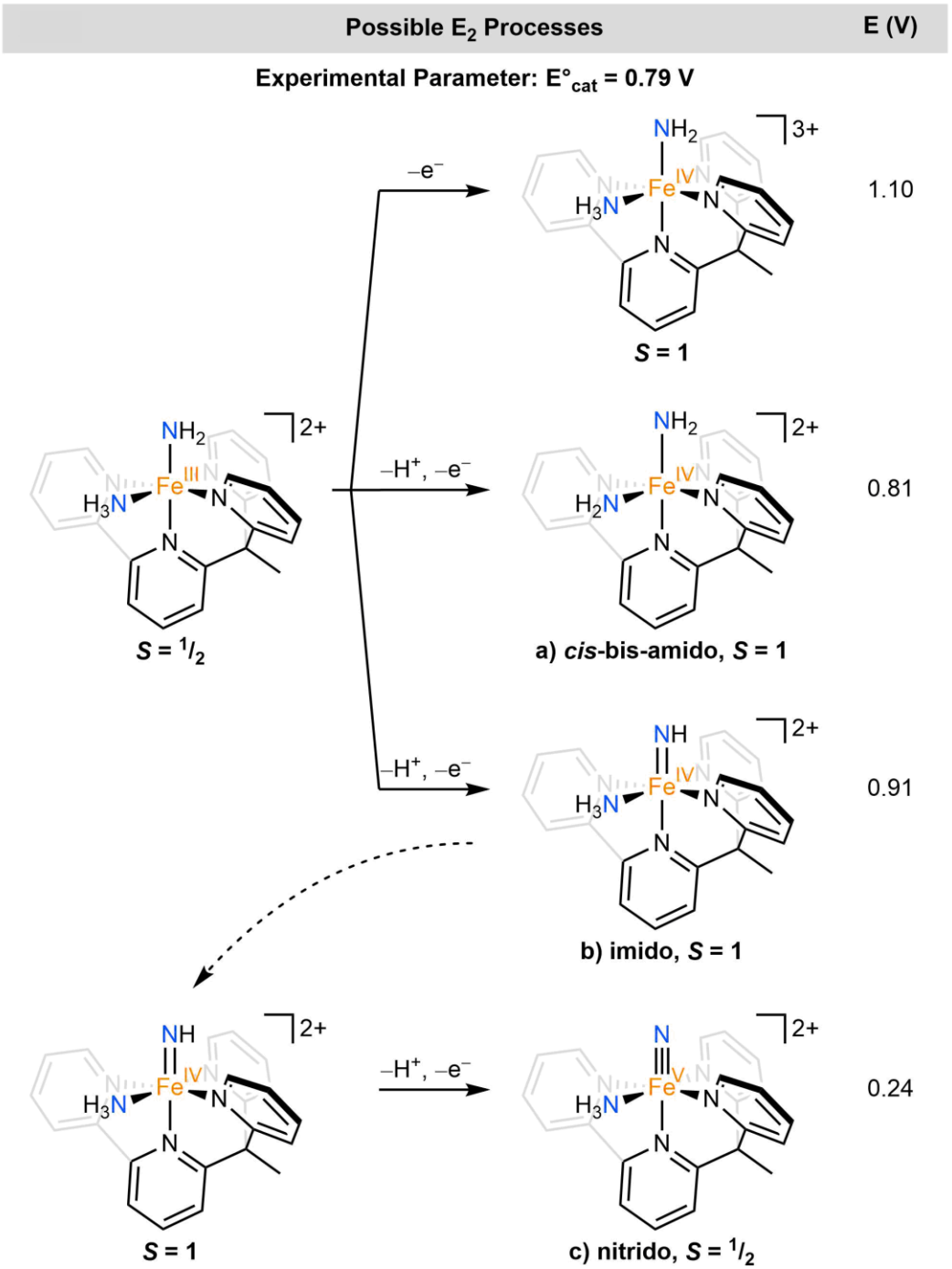

From the E_1 product, $[(bpyPy_2Me)Fe(NH_2)(NH_3)]^{2+}$, one can consider a subsequent 1-electron oxidation step that determines the E_2 potential (0.79 V by DPV). Calculations suggest oxidation to $[(bpyPy_2Me)Fe(NH_2)(NH_3)]^{3+}$ requires a potential of 1.10 V, well above 0.79 V. However, a proton-coupled oxidation step to instead generate a *cis*-bis-amido complex, $[(bpyPy_2Me)Fe(NH_2)(NH_2)]^{2+}$, occurs at 0.81 V (Scheme 4.3, (a)). Alternatively, a proton-coupled oxidation to generate the imido complex $[(bpyPy_2Me)Fe(NH)(NH_3)_2]^{2+}$ occurs at 0.91 V (Scheme 4.3, (b)), from which a subsequent proton-coupled oxidation to produce the nitride species $[(bpyPy_2Me)Fe(N)(NH_3)]^{2+}$ can occur at much lower potential (0.24 V, Scheme 4.3, (c)). On thermodynamic grounds, both scenarios remain plausible in working towards a mechanistic model.

We have also probed subsequent N–N bond formation steps. For example, we investigated both reductive elimination (I2N) from the *cis*-bis-amido and ANA from the imido/nitrido species; the first scenario highlights a *cis*-labile catalyst design, as in $[(bpyPy_2Me)Fe(MeCN)_2]OTf_2$. From $[(bpyPy_2Me)Fe(NH_2)(NH_2)]^{2+}$, N–N reductive elimination to form the η^2-hydrazine adduct $[(bpyPy_2Me)Fe(\eta^2\text{-}N_2H_4)]^{2+}$ (Scheme 4.4, (d)) is exergonic by 6.3 kcal/mol. Alternatively, ANA at either the imido or nitrido (Scheme 4.4, (e) and (f)) is exergonic by 16.0 or 28.7 kcal/mol, respectively, affording another plausible path towards N–N bond formation. Other pathways, such as those including bimolecular N–N coupling (e.g., from NH_2, NH, or N intermediates), may also be plausible (see SI for additional details).

Scheme 4.4. Possible N–N coupling reactions; ΔG (kcal/mol). DFT-predicted ground spin-state values are shown.

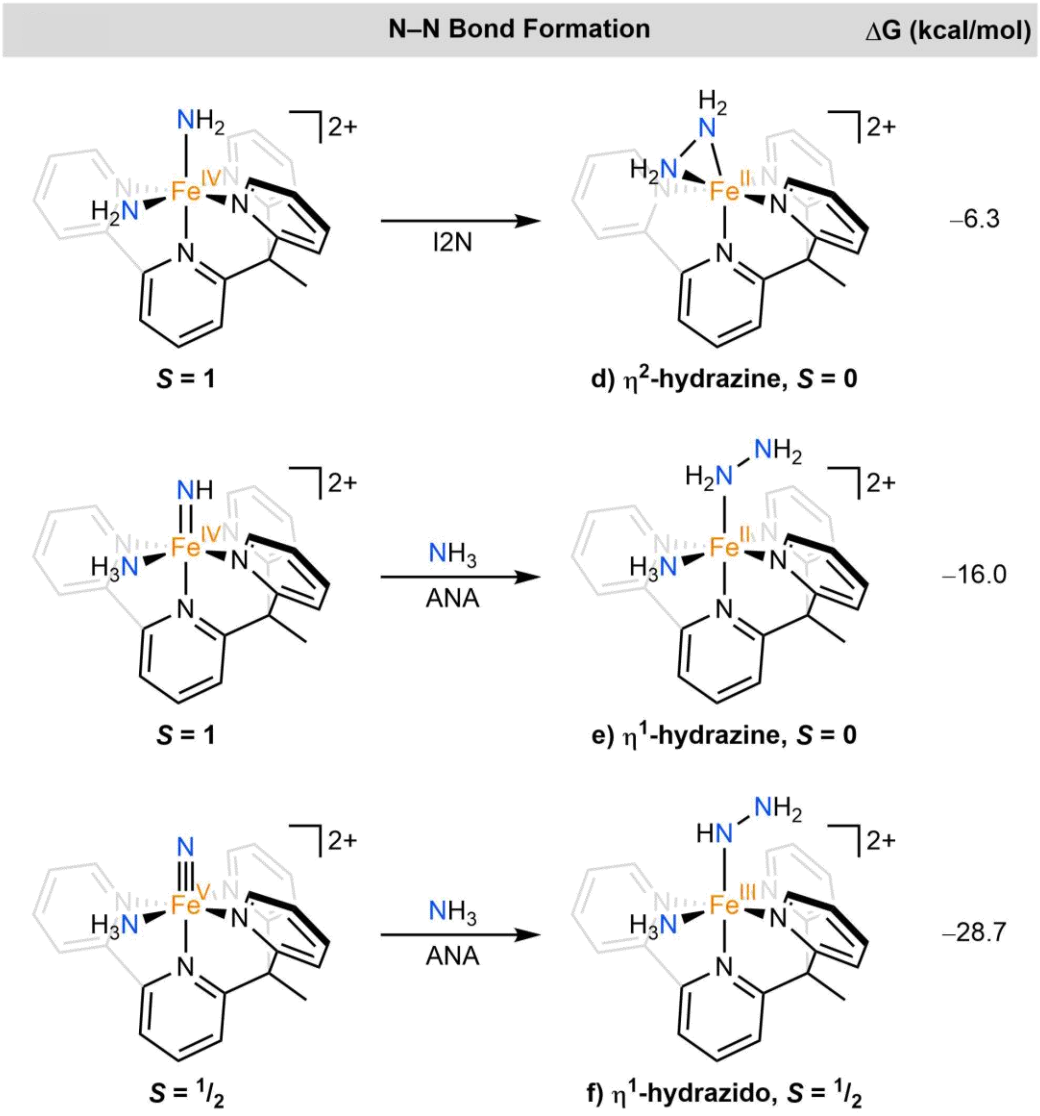

4.3 Conclusion

In conclusion, $[(bpyPy_2Me)Fe(MeCN)(NH_3)]OTf_2$ is an effective AO catalyst, yielding a net TON of 149 after 48 h, which is the highest TON value reported to date for a molecular catalyst. Compared to its related iron congener, $[(TPA)Fe(NH_3)_2]OTf_2$, $[(bpyPy_2Me)Fe(MeCN)(NH_3)]OTf_2$ is substantially more stable and operates at a higher rate

at significantly lower overpotential. While a number of mechanistic insights have been discussed, including a net H-atom abstraction at E_1 to furnish $[(bpyPy_2Me)Fe(NH_2)(NH_3)]^{2+}$ prior to the onset of catalysis at E_2, future efforts are needed to probe mechanistic aspects of the N–N bond-forming step(s), guided by the thermodynamic considerations from the experiments and theory discussed herein.

4.4 References

[1] Valera-Medina, A.; Xiao, H.; Owen-Jones, M.; David, W. I. F.; Bowen, P. J. Ammonia for Power. *Prog. Energ. Combust.* **2018,** *69*, 63–102.

[2] Zhao, Y.; Setzler, B. P.; Wang, J.; Nash, J.; Wang, T.; Xu, B.; Yan, Y. An Efficient Direct Ammonia Fuel Cell for Affordable Carbon-Neutral Transportation. *Joule* **2019,** *3*, 2472–2484.

[3] For a review on early work see: Nowak, E. J. Catalytic Oxidation of Ammonia on Platinum. *Chem. Eng. Sci*. **1966**, *21*, 19–27.

[4] Adli, N. M.; Zhang, H.; Mukherjee, S.; Wu, G. Review—Ammonia Oxidation Electrocatalysis for Hydrogen Generation and Fuel Cells. *J. Electrochem. Soc.* **2018**, *165*, J3130–J3147.

[5] de Vooys, A. C. A.; Koper, M. T. M.; van Santen, R. A.; van Veen, J. A. R. The Role of Adsorbates in the Electrochemical Oxidation of Ammonia on Noble and Transition Metal Electrodes. *J. Electroanal. Chem.* **2001**, *506*, 127–137.

[6] Li, Z.-F.; Wang, Y.; Botte, G. G. Revisiting the Electrochemical Oxidation of Ammonia on Carbon-Supported Metal Nanoparticle Catalysts. *Electrochim. Acta* **2017**, *228*, 351–360.

[7] Song, L.; Liang, Z.; Ma, Z.; Zhang, Y.; Chen, J.; Adzic, R. R.; Wang, J. X. Temperature-Dependent Kinetics and Reaction Mechanism of Ammonia Oxidation on Pt, Ir, and PtIr Alloy Catalysts. *J. Electrochem. Soc.* **2018**, *165*, J3095–J3100.

[8] Dunn, P. L.; Cook, B. J.; Johnson, S. I.; Appel, A. M.; Bullock, R. M. Oxidation of Ammonia with Molecular Complexes. *J. Am. Chem. Soc.* **2020**, *142*, 17845–17858

[9] Habibzadeh, F.; Miller, S. L.; Hamann, T. W.; Smith, M. R. Homogeneous Electrocatalytic Oxidation of Ammonia to N_2 Under Mild Conditions. *Proc. Natl. Acad. Sci. U.S.A.* **2019**, *116*, 2849–2853.

[10] Bhattacharya, P.; Heiden, Z. M.; Chambers, G. M.; Johnson, S. I.; Bullock, R. M.; Mock, M. T. Catalytic Ammonia Oxidation to Dinitrogen by Hydrogen Atom Abstraction. *Angew. Chem. Int. Ed.* **2019,** *58*, 11618–11624.

[11] Nakajima, K.; Toda, H.; Sakata, K.; Nishibayashi, Y. Ruthenium-Catalysed Oxidative Conversion of Ammonia into Dinitrogen. *Nat. Chem.* **2019**, *11*, 702–709.

[12] Zott, M. D.; Garrido-Barros, P.; Peters, J. C. Electrocatalytic Ammonia Oxidation Mediated by a Polypyridyl Iron Catalyst. *ACS Catal.* **2019,** *9*, 10101–10108.

[13] Dunn, P. L.; Johnson, S. I.; Kaminsky, W.; Bullock, R. M. Diversion of Catalytic C–N Bond Formation to Catalytic Oxidation of NH_3 through Modification of the Hydrogen Atom Abstractor. *J. Am. Chem. Soc.* **2020,** *142*, 3361–3365.

[14] As a convention, we define one turnover as the production of one equivalent of N_2 per catalyst equivalent.

[15] Lindoy, L. F.; Livingstone, S. E. Complexes of Iron(II), Cobalt(II) and Nickel(II) with α-Diimines and Related Bidentate Ligands. *Coord. Chem. Rev.* **1967**, *2*, 173–193.

[16] Phan, H.; Hrudka, J. J.; Igimbayeva, D.; Lawson Daku, L. M.; Shatruk, M. A Simple Approach for Predicting the Spin State of Homoleptic Fe(II) Tris-Diimine Complexes. *J. Am. Chem. Soc.* **2017**, *139*, 6437–6447.

[17] Ashley, D. C.; Jakubikova, E. Tuning the Redox Potentials and Ligand Field Strength of Fe(II) Polypyridines: The Dual π-Donor and π-Acceptor Character of Bipyridine. *Inorg. Chem.* **2018**, *57*, 9907–9917.

[18] Chen, K.; Que, L. Stereospecific Alkane Hydroxylation by Non-Heme Iron Catalysts: Mechanistic Evidence for an Fe^{V}=O Active Species. *J. Am. Chem. Soc.* **2001**, *123*, 6327–6337.

[19] Que, L., Jr.; Tolman, W. B. Biologically Inspired Oxidation Catalysis. *Nature* **2008**, *455*, 333–340.

[20] Fillol, J. L.; Codolá, Z.; Garcia-Bosch, I.; Gómez, L.; Pla, J. J.; Costas, M. Efficient Water Oxidation Catalysts Based on Readily Available Iron Coordination Complexes. *Nat. Chem.* **2011**, *3*, 807−813.

[21] Chen, L.; Su, X.-J.; Jurss, J. W. Selective Alkane C–H Bond Oxidation Catalyzed by a Non-Heme Iron Complex Featuring a Robust Tetradentate Ligand. *Organometallics* **2018**, *37*, 4535–4539.

[22] Khnayzer, R. S.; Thoi, V. S.; Nippe, M.; King, A. E.; Jurss, J. W.; El Roz, K. A.; Long, J. R.; Chang, C. J.; Castellano, F. N. Towards a Comprehensive Understanding of Visible-Light Photogeneration of Hydrogen from Water Using Cobalt(II) Polypyridyl Catalysts. *Energy Environ. Sci.* **2014**, *7*, 1477–1488.

[23] Pegis, M. L.; Wise, C. F.; Koronkiewicz, B.; Mayer, J. M. Identifying and Breaking Scaling Relations in Molecular Catalysis of Electrochemical Reactions. *J. Am. Chem. Soc.* **2017**, *139*, 11000–11003.

[24] Azcarate, I.; Costentin, C.; Robert, M.; Savéant, J.-M. Through-Space Charge Interaction Substituent Effects in Molecular Catalysis Leading to the Design of the Most Efficient Catalyst of CO_2-to-CO Electrochemical Conversion. *J. Am. Chem. Soc.* **2016**, *138*, 16639–16644.

[25] As previously reported,[12] $FeOTf_2$ itself is rapidly deposited on the electrode and produces minimal N_2; a reload experiment shows no activity. At the low applied bias used in this work, N_2 levels are too low to be quantified in the absence of iron sources.

[26] Costentin, C.; Savéant, J.-M. *Elements of Molecular and Biomolecular Electrochemistry: An Electrochemical Approach to Electron Transfer Chemistry*, 2nd ed.; John Wiley & Sons: Hoboken, NJ, 2006.

[27] Savéant, J.-M.; Vianello, E. Potential-Sweep Voltammetry: General Theory of Chemical Polarization. *Electrochim. Acta* **1967**, *12*, 629−646.

[28] Costentin, C.; Drouet, S.; Robert, M.; Savéant, J.-M. Turnover Numbers, Turnover Frequencies, and Overpotential in Molecular Catalysis of Electrochemical Reactions. Cyclic Voltammetry and Preparative-Scale Electrolysis. *J. Am. Chem. Soc.* **2012**, *134*, 11235−11242.

[29] Wang, V. C.-C.; Johnson, B. A. Interpreting the Electrocatalytic Voltammetry of Homogeneous Catalysts by the Foot of the Wave Analysis and Its Wider Implications. *ACS Catal.* **2019**, *9*, 7109−7123.

[30] Buhr, J. D.; Taube, H. Oxidation of $[Os(NH_3)_5CO]^{2+}$ to $[(Os(NH_3)_4CO)_2N_2]^{4+}$. *Inorg. Chem.* **1979**, *18*, 2208−2212.

[31] Abbenseth, J.; Finger, M.; Würtele, C.; Kasanmascheff, M.; Schneider, S. Coupling of Terminal Iridium Nitrido Complexes. *Inorg. Chem. Front.* **2016**, *3*, 469–477.

[32] Keener, M.; Peterson, M.; Hernandez Sanchez, R.; Oswald, V. F.; Wu, G.; Menard, G. Towards Catalytic Ammonia Oxidation to Dinitrogen: A Synthetic Cycle by Using a Simple Manganese Complex. *Chem. - Eur. J.* **2017**, *23*, 11479−11484.

[33] Collman, J. P.; Hutchison, J. E.; Ennis, M. S.; Lopez, M. A.; Guilard, R. Reduced Nitrogen Hydride Complexes of a Cofacial Metallodiporphyrin and Their Oxidative Interconversion. An Analysis of Ammonia Oxidation and Prospects for a Dinitrogen Electroreduction Catalyst Based on Cofacial Metallodiporphyrins. *J. Am. Chem. Soc.* **1992**, *114*, 8074−8080.

[34] Gu, N. X.; Oyala, P. H.; Peters, J. C. Hydrazine Formation via Coupling of a Nickel(III)–NH_2 Radical. *Angew. Chem. Int. Ed.* **2021**, *60*, 4009–4013.

[35] Siig, O.; Kepp, K. Iron(II) and Iron(III) Spin Crossover: Toward an Optimal Density Functional. *J. Phys. Chem. A* **2018**, *122*, 4208–4217.

[36] See SI for full details. Calculations considered all possible spin multiplicities and plausible isomers.